Phase and structural changes during heat treatment of additive manufactured CrFeCoNi high-entropy alloy

Yulia O. Kuzminova [a,*], Egor A. Kudryavtsev [b], Jae-Kyung Han [c], Megumi Kawasaki [c], Stanislav A. Evlashin [a]

[a] Center for Design, Manufacturing & Materials, Skolkovo Institute of Science and Technology, Moscow 121205, Russia
[b] The Joint Research Center of Belgorod State National Research University «Technology and Materials», Belgorod 308015, Russia
[c] School of Mechanical, Industrial & Manufacturing Engineering, Oregon State University, Corvallis, OR 97331, USA

ARTICLE INFO

ABSTRACT

Additive manufacturing (AM) of high-entropy alloys (HEAs) is a new challenge in the Material Science and Advanced Manufacturing fields. In the AM processing procedure, heat treatments after fabrication are often beneficial to stabilize microstructure and properties, while limited reports are available for AM HEAs. In the current study, the effect of a post-printing heat treatment at 400–1000 ℃ for 24 h and for 21 days on the changes in structures and phase compositions of an AM CrFeCoNi alloy prepared by the laser powder bed fusion AM technique is presented to better understand a heat treatment-microstructure-property relationship of the AM HEA. Heating up to 600 ℃ demonstrated the polygonization process in the alloy. Grain growth was observed in the alloy upon heating over 700 ℃, while a preferred texture is observed along the build direction after annealing at 900 ℃ for 24 h. The formation of the secondary phase was revealed, and it is associated with the impurities of the initial CrFeCoNi powder. The AM CrFeCoNi system demonstrates excellent phase stability inthe solid solution for all annealing temperatures.

© 2021 Elsevier B.V. All rights reserved.

1. Introduction

High-entropy alloys (HEAs) have received great attention in materials science due to their new alloy-design approach in comparison with the conventional alloy developments. Earlier terminology of HEA was used for expressing a single solid solution [1,2]. However, Miracle and Senkov reviewed that the essential group of HEAs contains at least two phases [3]. The presence of secondary phases provides a tangible impact on the mechanical and physical properties of HEAs. For example, a B2/body-centered cubic (bcc) phase formed by the presence of Al increases the strength characteristics [4–6] as well as the thermal and electrical properties [7] in AlCoCrFeNi alloys. Moreover, precipitations of the σ-phase nucleated at elevated temperatures of 600–800 ℃ increase strength in $Al_{0.5}CoCrFeMnNi$ and CoCrFeMnNi alloys [8,9]. A detailed investigation in the phase stability of a CoCrFeMnNi alloy demonstrated the formation of a Cr-rich bcc phase, Fe-Co phase, and Ni-Mn $L1_0$ structure at a temperature range of 500–600 ℃ [9–11]. A stable face-centered cubic (fcc) solid solution of a CoCrFeMnNi alloy is observed only at temperatures higher than 800 ℃ [11], while an ultrafine-grained CoCrFeNi alloy without Mn provides a stable solid solution after heating up to ~730 ℃ [12]. By contrast, Sathiyamoorthi et al. observed the evolution of Cr_7C_3 particles in a CoCrFeNi alloy at 600 ℃ up to 1000 ℃ [13] and the observed phase was expected as the σ-phase [14].

HEAs are actively constructed through the application of the modern manufacturing techniques such as Additive Manufacturing (AM) [15,16]. For the AM process, post-printing heat treatment of the as-built materials is often applied to remove residual stresses, but it leads to structural changes including recrystallization and secondary phase formations [17–19]. Synthesis of CoCrFeMnNi alloys is common by the AM process due to their nature with a ductile fcc structure as matrix, which provides stable printability [19–21]. A CrFeCoNi alloy also demonstrates the same or even better properties than the five-component alloy [22–25]. The four-component system is actively explored for composition modification by the AM process [26,27]. However, the results obtained from structural and phase analyses are contradictory for the quaternary CoCrFeNi alloy, while the microstructural and phase thermal stabilities are well investigated for the CoCrFeMnNi alloys. Therefore, a comprehensive understanding of the influence of temperature in the post-printing

---

* Correspondence to: Skolkovo Institute of Science and Technology, Bolshoy Boulevard 30, bld. 1, Moscow 121205, Russia.

E-mail address: yulia.kuzminova@skoltech.ru (Y.O. Kuzminova).

Table 1
The chemical composition of CrFeCoNi powder in wt%.

Cr	Fe	Co	Ni	O	N	C
24.65	25.09	25.47	24.55	0.129	0.095	0.015

Table 2
A list of the applied printing process parameters.

L-PBF parameter	Values
Laser power	150 W
Laser spot diameter	55 μm
Hatch spacing	80 μm
Layer thickness	20 μm
Laser scan speed	600 mm/s
Gas speed (Ar)	2.5 m/s
Oxygen level	< 0.3 at%
Pressure in chamber	1 bar

heat treatment on CoCrFeNi alloy is required for the development of the desirable HEAs having stable structure produced by the current AM techniques.

Accordingly, the present research demonstrates a comprehensive study of structural evolution during post-printing heat treatment of an AM CrFeCoNi alloy over a wide temperature range of 400–1000 ℃.

2. Material and methods

2.1. Material

The CrFeCoNi powder (JSC Polema, Russia) with purity of > 99.7 wt% obtained through a spraying technique was used in the study. Table 1 summarizes the full chemical composition of the powder. Fig. 1 presents (a) the low and (b) high magnifications of the powder morphology. According to previous powder analysis, the particle size distribution poses in a range of 10–60 μm with average size of 27 μm [23]. The particles were predominantly spherical, while some particles had irregular shapes.

2.2. Printing process

The CrFeCoNi alloy was performed using the widely used laser powder bed fusion (L-PBF) additive manufacturing technique. TruPrint 1000 metal 3D printer (TRUMPF) was used in the current work to manufacture the samples with the selected printing process parameters according to the results from the previous study [18]. A full list of the applied parameters is shown in Table 2. The samples were printed with the chess X-Y scan strategy with a square side of 4 mm (detailed information of the applied scan strategy is described

elsewhere [28]). Totally, 10 cylindrical samples were printed with a diameter and a height of 10.0 mm and 10.0 mm, respectively. The printing process was conducted without platform preheating.

2.3. Heat treatment process

The printed samples were annealed at different temperatures in the range of 400–1000 ℃ with a step of 100 ℃ in air. The cylindrical samples were disposed of in the furnace SNOL 6.7-1300 (AB UMEGA GROUP) preheated to the required temperature. Each sample was annealed for 24 h with the following cooling in water. Additionally, the long heat treatment in air was applied to the as-built samples at temperatures of 600 and 700 ℃ for 21 days.

2.4. Differential scanning calorimetry

Thermal stability of the CrFeCoNi powder and the as-built CrFeCoNi sample was studied using differential scanning calorimetry (DSC) analysis using the thermal analyzer STA 449 F3 Jupiter (NETZSCH) with a heating speed of 20 K/min up to 900 ℃ in Ar atmosphere.

2.5. Microhardness testing

Top sample surfaces were prepared for the microhardness tests with the 2000-grit SiC papers. A Vickers microhardness testing
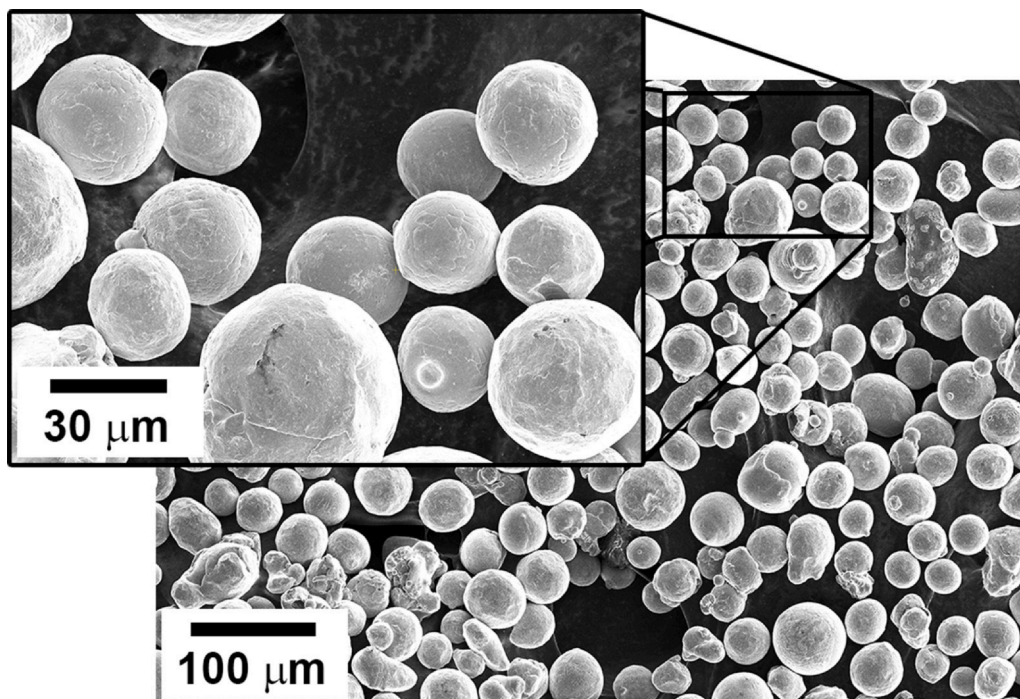

Fig. 1. SEM images of the CrFeCoNi powder at low and high magnifications.

machine ITV-1-AM (Metrotest, Russia) was used for the micro-hardness tests under a load of 300 g for at least 10 measurements per sample.

2.6. Structural and phase analyses

Structural analysis was performed using a scanning electron microscope Quattro S (Thermo Fisher Scientific Inc., USA) equipped with an energy dispersive X-ray (EDX) detector. The samples were cut perpendicularly to the build direction, ground using the SiC grinding papers up to 2000-grit, and polished with a diamond suspension (up to 3 μm) and silica oxide suspension (up to 40 nm). A transmission electron microscope (TEM) JEM-2100 (JEOL, Japan) was used for the microstructural and phase analyses with the accelerating voltage of 200 kV. The samples were prepared by cutting transversely to the build direction and thinned up to 100 μm using the SiC grinding papers. The mixture of 95% CH_3COOH and 5% $HClO_4$ at the 25 V potential was applied for the twin-jet electropolishing using TenuPol5 machine (Struers, Denmark). To minimize the edge effect, all structural investigations were made in the sample centers. The analysis of light elements was performed using determinators LECO TC-136 and LECO SC-144 (LECO Corporation, USA). The structural calculations from images were made using the open source software ImageJ developed by National Institute of Health (USA).

Bruker D8 ADVANCE (Bruker, USA) diffractometer with CoKα radiation (wavelength = 1.79026 Å) was applied for performing the X-ray diffraction (XRD) analysis. The top surfaces of the samples was polished with the 2000-grit SiC grinding paper, polished with the final silica oxide suspension of 40 nm, and electropolished with LectroPol-5 (Struers, Denmark) using a solution of 900 ml C_4H_9OH + 100 ml $HClO_4$ at the ~28 V potential. The XRD patterns were obtained in the 2θ range from 47°–125° with a step size of 0.07° and an incremental time of 2.0 s.

3. Results

3.1. Thermal analysis and hardness evolution of CrFeCoNi alloy

[Fig. 2](#) presents the DSC traces from 200 °C to 900 °C for the powder and the bulk as-built samples of the CrFeCoNi alloy. The curve for the as-built sample has two endothermic peaks at ~500 °C and ~610 °C overlapping each other. The first peak begins at 400 °C with a peak at 500 °C, and it switches to the next peak with the

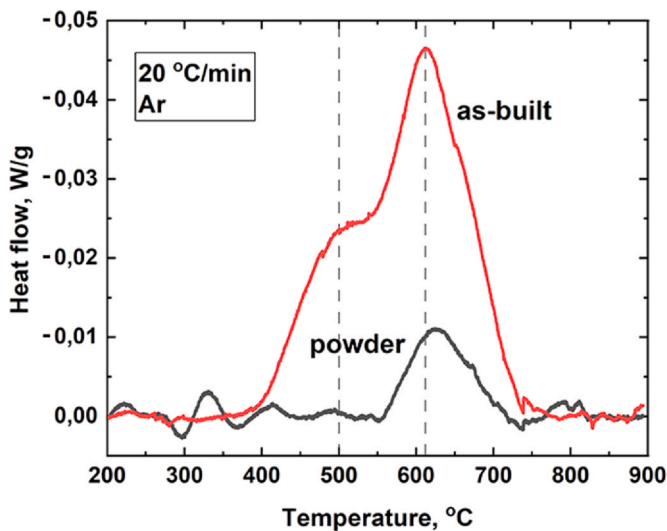**Fig. 2.** DSC thermograms obtained for the powder and as-built sample of AM CrFeCoNi at heating rate 20 °C/min in an argon atmosphere.
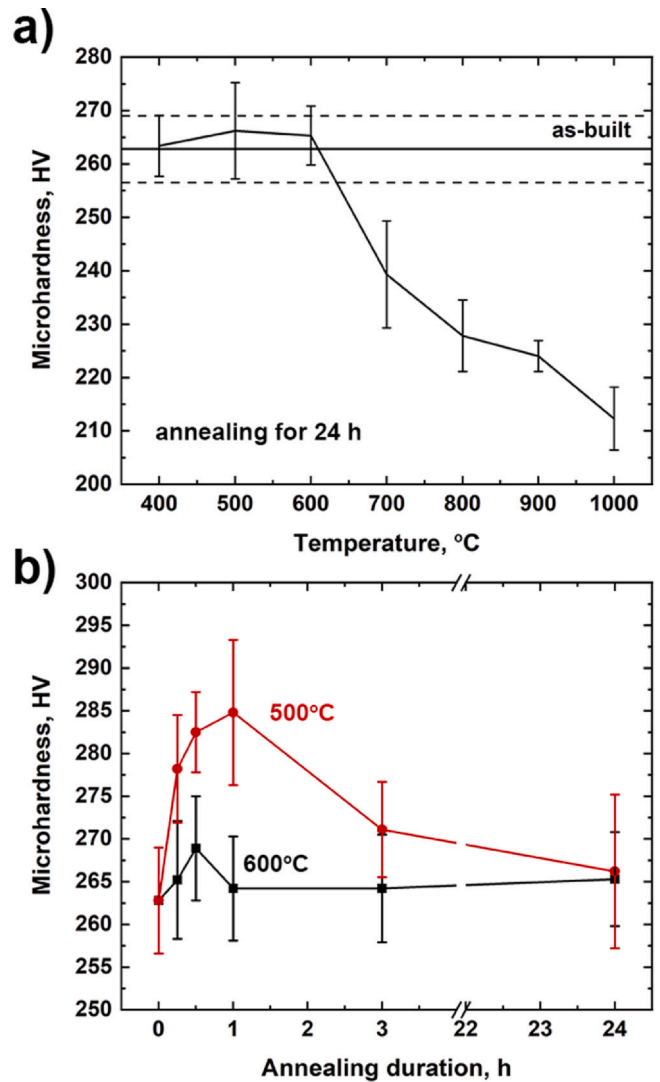
Fig. 3. Effect of (a) temperature and (b) duration of annealings at 500 and 600 °C on microhardness of AM CrFeMnNi alloy. The microhardness of as-built CrFeMnNi alloy in [Fig. 3](#)a is presented as the horizontal line and its standard deviation error as dotted lines.

highest at 610 °C and a finish at 740 °C. The powder sample shows only one peak starting at 550 °C and a finish at 740 °C, where the single peak seems consistent with the second peak of the as-built sample but with less intensity.

The connected first and second peaks of the exothermic peaks may be attributed to the recovery and recrystallization of the as-built CrFeCoNi alloy. Specifically, the first peak is related to the recovery process. The second peak for the as-built sample and the only distinguishable peak for the powder are associated with the recrystallization process. The highly strained as-built sample may provide the thermal peak shifting to lower temperatures in comparison to the powder sample. It is worth noting that an ultrafine-grained conventionally-manufactured CrFeCoNi alloy demonstrated the exothermic DSC peaks at 407 °C and 597 °C [12]. Considering the highly strained ultrafine-grained condition leading to the lower DSC peaks, the present as-built CrFeCoNi alloy demonstrated reasonable thermal characteristics. The integration of the thermal peak area yields 4.8 J/g for the powder and 6.8 J/g and 22.5 J/g for the first and the second peaks, respectively, for the as-built sample according to Gaussian peaks fitting.

[Fig. 3](#) shows the effect of (a) annealing temperature for 24 h of heating and (b) duration of annealings at 500 and 600 °C for 24 h on
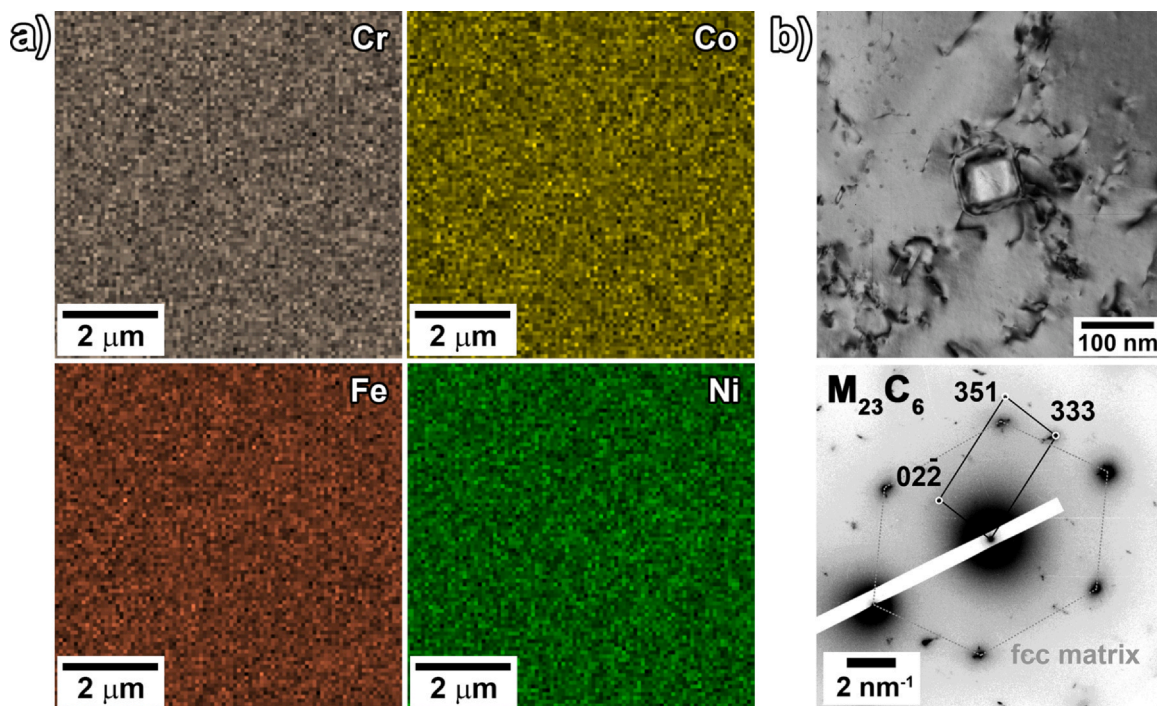
Fig. 4. (a) The homogeneous element distribution and (b) TEM image of M$_{23}$C$_6$ precipitate with a corresponding diffraction in the as-built CrFeCoNi alloy. (For interpretation of the references to color in this figure legend, the reader is referred to the web version of this article.)

microhardness of the AM CrFeCoNi alloy. Hardness of the as-built sample before annealing is ~263 HV that is denoted with a solid horizontal line with the error values with the dotted-lines in Fig. 3a. After annealing at 400 ℃, the hardness is similar compared with the as-built sample, and it reaches 267 HV at 500-600 ℃ which is higher than the as-built condition. Thereafter, hardness showed a continuous drop towards ~212 HV with increasing annealing temperature to 1000 ℃. The short annealing at 500 ℃ increases the material hardness which achieves the highest value of ~285 HV after 1 h and further decreases toward 267 HV after 24 h, Fig. 3b. The hardness measurements during annealing at 600 ℃ demonstrate the highest microhardness value after 30 min and a slight decrease after 1 h, which is then maintained consistent up to 24 h of annealing.

3.2. Microstructural evolution upon the annealing

Fig. 4 represents (a) the homogeneous element distributions taken by EDX analysis with no proof of secondary phase in the as-built CrFeCoNi alloy, while (b) the TEM image with corresponding TEM diffraction is indicating a presence of nano-scale M$_{23}$C$_6$ precipitates [29] in the material. Fig. 5 consists of the backscattered electron (BSE) images transversally to the build direction (BD) with two different magnifications of (a, b) the as-built CrFeCoNi alloy before annealing and after annealing at (c, d) 400 ℃ and (e, f) 500 ℃ for 24 h, and the TEM images of the CrFeCoNi alloy in (g) an as-built condition and (h) after annealing at 400 ℃. The as-built sample demonstrates the bimodal grain size distributions (Fig. 5a) where there are coarse grains with lengths of ~50 μm and widths of ~8 μm elongated transversally to the moving of the melt pool and a fine-grained structure between the neighboring melt tracks. The domains in the fine structure consist of subgrains (Fig. 5b) where a cellular substructure consists of elongated subgrains having a width of ~450 nm and a length of ~700 nm (Fig. 5g). Such cellular structure is responsible for higher strength characteristics in AM materials [30–32]. Note that the subgrains form a columnar structure following the build direction, where the elongation indicates their

growth oblique to the build direction [33]. The microstructure remained reasonably consistent after annealing at 400 ℃ (Fig. 5c) where both elongated and fine grains are still visible and the consistent substructure with average size of ~480 nm is observed with the formation of dislocation walls (Fig. 5d and h). After annealing at 500 ℃ for 24 h, the square domains with sizes of ~35 μm appear and the elongated structure appears to be ambiguous (Fig. 5e), while the cell substructure after annealing at 500 ℃ remains consistent with the materials in as-built and as-annealed at 400 ℃ (Fig. 5f).

Fig. 6 shows the microscopic images of the AM CrFeCoNi alloy after annealing at (a, b) 600 ℃, (c, d, e) 700 ℃, and (f) 800 ℃ for 24 h. Annealing at 600 ℃ leads to the polygonization process. In practice, the polygonized domains with smooth borders appear next to the fine structure (Fig. 6a), while the cellular substructure with cells of ~450 nm is formed within the domains (Fig. 6b). Note, the size of such domains having the length of ~55 μm and thickness of ~7 μm is similar to as-built structure. An increase in the annealing temperature towards 700 ℃ shows recrystallized grains in the entire fine grain regions with average size of ~1.5 μm, while the melt track with the elongated grains is inherited in some local regions (Fig. 6c). In higher magnification, secondary phase precipitates are observed at grain borders and these are denoted by white arrows (Fig. 6d). The TEM image presents a degradation of cellular structure and dislocation-free grains in the regions where recrystallization occurs (Fig. 6e). The dislocation walls of the substructure are degraded, and, instead, the dislocations migrate to grain borders and some subgrains coalesce. The BSE image of the AM CrFeCoNi alloy annealed at 800 ℃ reveals the further developed recrystallization process and the impedance of the grain borders coalescence by the secondary phase precipitates that are marked by white arrows (Fig. 6f). After 800 ℃ annealing, the grain size of the substructure is in the range of 0.5–3.3 μm. It should be mentioned that due to high irregularity of the microstructure after annealing at 700 and 800 ℃, the estimation of the precise grain sizes is complicated.

Fig. 7 presents the BSE images of the AM CrFeCoNi alloy followed by annealing for 24 h at (a) 900 ℃ and (b, c) 1000 ℃, and (d) a TEM
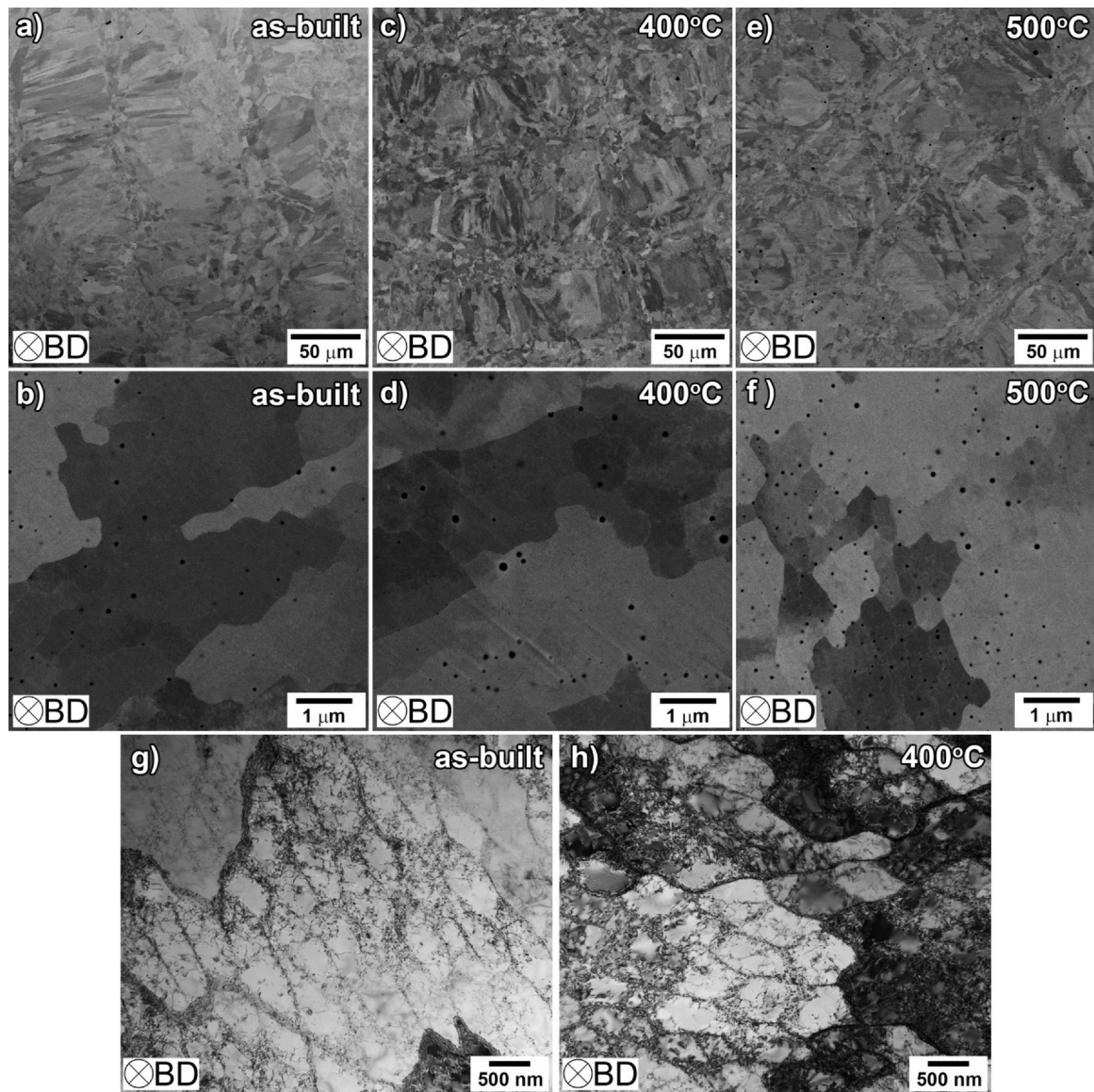
Fig. 5. BSE images of (a, b) as-built CrFeCoNi alloy and after annealing at (c, d) 400 and (e, f) 500 ℃ for 24 h and TEM images of (g) as-built and (h) annealed at 400 ℃ CrFeCoNi alloy.

image of the as-annealed alloy at 900 ℃. After annealing at 900 ℃, newly formed large grains with size of 5–10 µm are visible in the formally fine-grained region (Fig. 7a). As seen in the depicted image in Fig. 7a, the formation of recrystallized small grains also occurs (marked by white arrows). The domain walls are formed by the dissolved subgrain borders consisting of dislocations, which are visible in the TEM micrographs where the dissolved subgrain borders promote dislocation pile-ups and intragranular dislocations are visible in the observed region of the alloy after annealing at 900 ℃ (Fig. 7d). After 900 ℃ annealing, the average size of microstructure is ~1260 nm. The bimodal microstructure is still observed after annealing at 1000 ℃ in the AM CrFeCoNi alloy (Fig. 7b), while the high magnification micrograph shows a replacement of the fine structure to the equiaxed recrystallized grains with sizes of ~0.5–2.5 µm (Fig. 7c).

In previous works, the precipitates observed in a CrFeCoNi microstructure after annealing at 750 ℃ and 800 ℃ are considered as the σ-phase [18,23]. In order to examine detailed structure of the secondary phase in the alloy heated at different temperatures and treatment time, TEM diffraction analysis was performed for the alloy

after annealing for 24 h. Fig. 8 shows TEM diffractions for the precipitates observed in the AM CrFeCoNi alloy after annealing at (a) 700 ℃ and (b) 900 ℃. The analysis reveals that the consistent M_2N structure [34] presents in both samples. The presence of the secondary phase is further confirmed by a long-term heat treatment at 700 ℃ for 21 days leading to the coarsening of the precipitates in the as-built CrFeCoNi alloy and it is available by EDX analysis as shown in Fig. 9a. It was determined that the precipitates are rich in Cr (up to 50 at%) with an equal value of other elements and high values of N and O. Table 3 presents the detailed composition of spots presented in Fig. 9a. Moreover, the as-built CrFeCoNi alloy was also heat treated at 600 ℃ for 21 days to evaluate the presence of the secondary phase with the M_2N structure during the recrystallization process at 600 ℃, and a BSE image of the CrFeCoNi sample is shown in Fig. 9b. The formation of Cr-rich precipitates were visible along grain boundaries after the long heat treatment at 600 ℃. Note that the formation of the secondary phase may affect the recrystallization behavior of the as-built CrFeCoNi alloy. The analysis of N content was performed using a combustion method due to the low effectiveness of EDX method for the analysis of light elements. As it was presented in
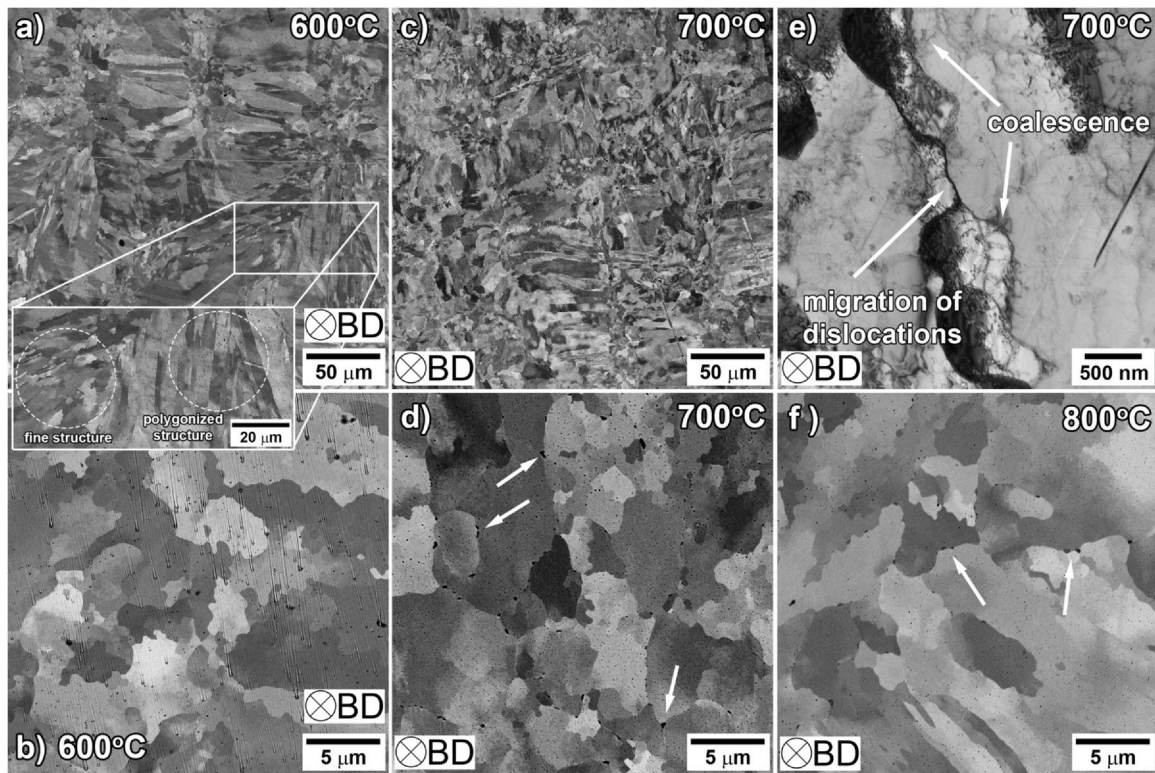
Fig. 6. The images of CrFeCoNi structures after annealing at temperatures of (a, b) 600 ℃, (c, d, e) 700 ℃, and (f) 800 ℃. All images are BSE except the 6e which is represented as a TEM micrograph.
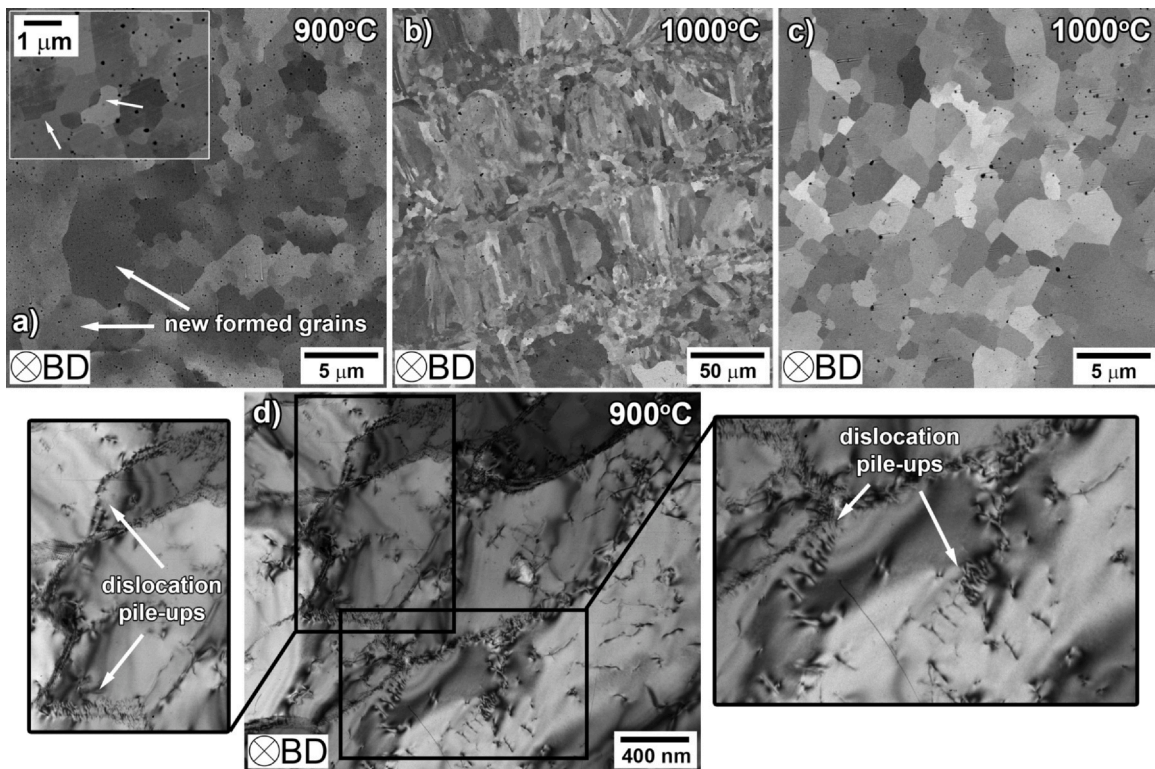

Fig. 7. BSE images of AM CrFeCoNi alloy after annealing at (a) 900 and (b, c) 1000 ℃ and (d) the TEM image of as-annealed at 900 ℃ CrFeCoNi alloy.
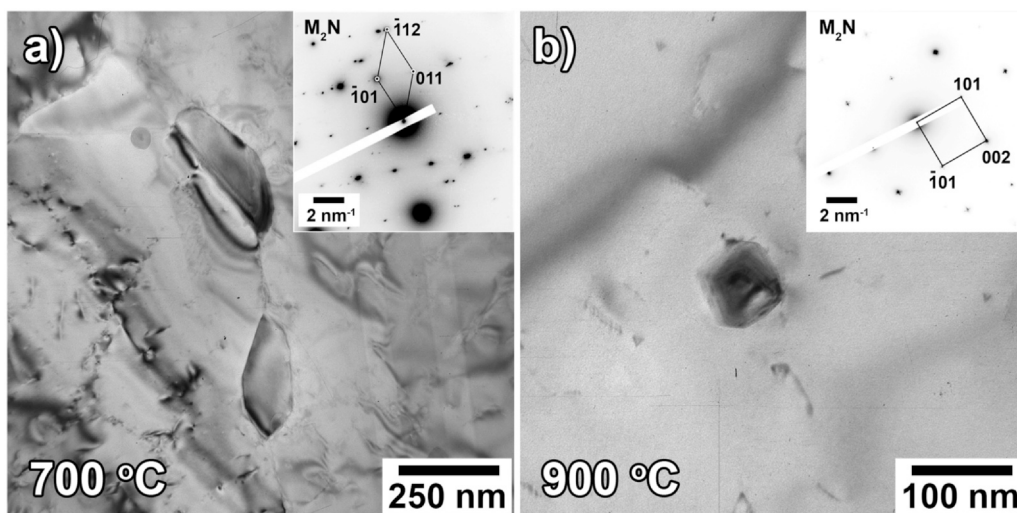
Fig. 8. TEM diffraction of precipitates found at the AM CrFeCoNi after annealing at (a) 700 and (b) 900 ℃.
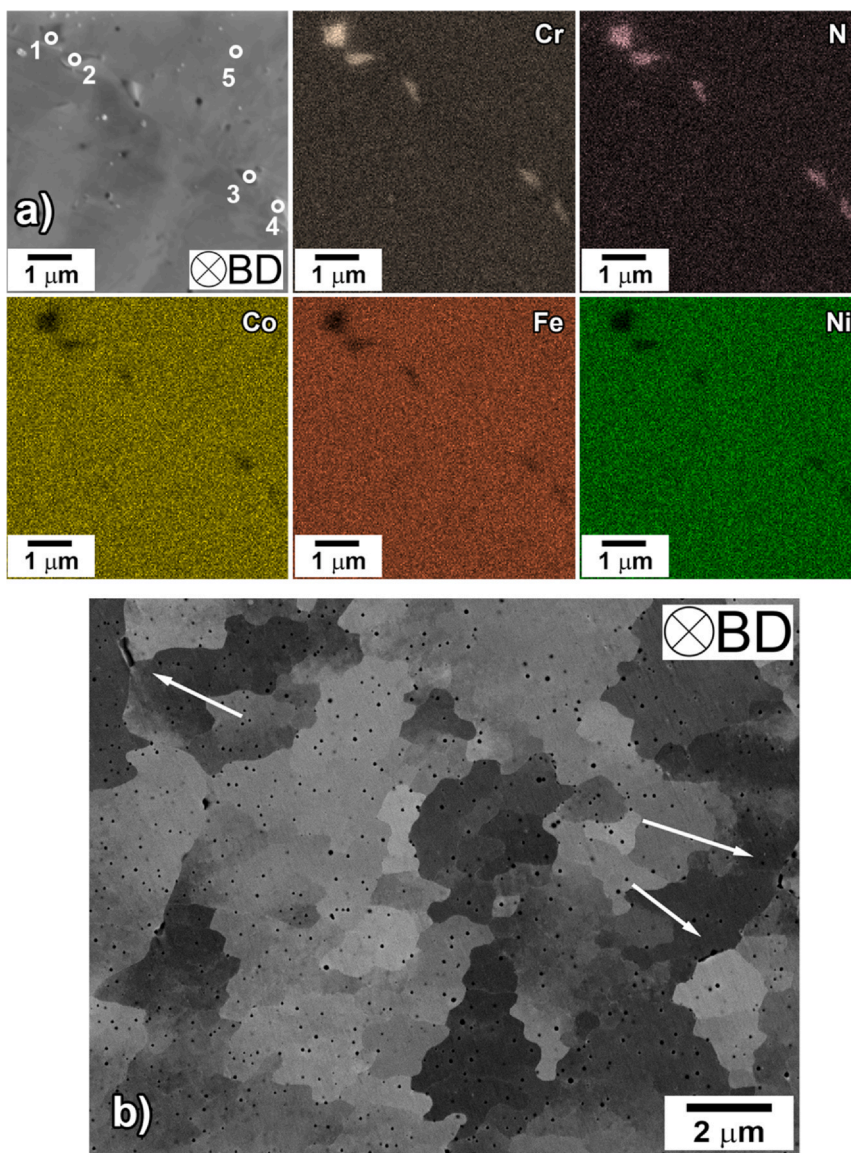

Fig. 9. (a) EDX result of AM CrFeCoNi alloy annealed at 700 ℃ for 21 days; (b) BSE image of AM CrFeCoNi alloy annealed at 600 ℃ for 21 days. (For interpretation of the references to color in this figure legend, the reader is referred to the web version of this article.)

Table 3
The chemical composition (in wt%) of CrFeCoNi alloy annealed at 700 °C for 21 days estimated with EDX. The number of points corresponds to the locations with the consistent numbers in Fig. 9a.

	C	O	N	Cr	Fe	Co	Ni
spot 1	7.42	**13.53**	**4.76**	**48.20**	9.79	8.61	7.69
spot 2	7.60	**11.94**	**4.28**	**40.10**	13.08	12.07	10.93
spot 3	6.58	**10.36**	**4.28**	**33.92**	16.01	15.12	13.73
spot 4	7.45	**9.13**	**4.16**	**29.98**	17.33	16.44	15.51
spot 5	7.32	1.22	2.89	22.73	22.77	21.99	21.08

Table 1, 0.095 wt% of N in the powder was determined. There is relatively the same content of N (~0.085 wt%) in the printed samples before heat treatment and after annealing at 700 °C for 24 h as well as 21 days. After printing, the contents of O and C in the material also drop toward ~0.115 and ~0.004 wt%, respectively, and stay at approximately the same level after the annealing at 700 °C up to 21 days.

Fig. 10 presents (a) the X-ray profiles of the powder, the as-built CrFeCoNi alloy before and after annealing at 400, 700, and 900 °C for 24 h and the BSE images of CrFeCoNi alloy at (b) as-printed and (c) as-annealed at 1000 °C for 24 h conditions. According to XRD analysis, all samples present a pure fcc structure, Fig. 10a. The dotted lines indicate the interplanar distance for corresponding planes for the crystal structure with a lattice parameter of 3.58 Å. In contrast to compositional analysis, no additional phases such as $M_{23}C_6$ precipitates and Cr-rich precipitates with M_2N structure were determined both before and after annealing due to their small contents below ~5 vol%, which is the XRD detection limit. Only the powder profile reveals the dominant (111) peak, while all other profiles for as-built samples demonstrate the strong texture of < 100 > and < 110 > toward the build direction. It is reported for the 316l stainless steel having an fcc structure the < 110 > crystal texture alignments with the build direction and the < 100 > crystal texture with the laser track [33]. In the current study with the CrFeCoNi alloy, the difference in the XRD peak intensity is associated with the texture variety between the < 100 > and < 110 > along the printed sample heights, and the tendency is maintained after annealing at 900 °C for 24 h. As can be seen in Fig. 10b and c, the preferable texture is observed even after 1000 °C annealing for 24 h.

4. Discussion

4.1. Structural evolution

DSC analysis demonstrates two endothermic peaks for the as-built CrFeCoNi alloy at 500 and 610 °C. The first peak is associated with the recovery process in the material, which agrees with the results of SEM analysis revealing no structural changes up to 600 °C. The second DSC peak at 610 °C ending at 740 °C is associated with the following two processes. The first process is related to the beginning of the recrystallization of the material. At 700 °C, the grains grow and degradation of dislocation walls are observed in the material. The second process is associated with the secondary phase formation, where TEM and EDX analyses demonstrated the appearance of the Cr-rich precipitates with M_2N structure at the temperature range of 700–800 °C after heating for 24 h. It should be noted that the long heat treatment at lower temperature can also form the nitrides in CrFeCoNi alloy, as shown in Fig. 9b. Thus, the contributions of the recrystallization process and the secondary phase formation process to the second DSC peak can be influenced by the heat treatment conditions. Note, Sathiyamoorthi et al. performing the DSC analysis on mechanically alloyed CoCrFeNi powder observed the exothermic peak at 600 °C, which was associated with the appearance of Cr_7C_3 precipitates [13]. In the present study, the carbides with $M_{23}C_6$ structure were observed in the as-built condition (Fig. 4b). Shun and Du considered the decomposition of the Cr_7C_6 carbide to $Cr_{23}C_6$ in $Al_{0.3}CoCrFeNiC_{0.1}$ alloy at temperatures of 800–1000 °C [35]. The presence of both carbide types is possible in the current AM CrFeCoNi. However, in contrast to the studies [13,35], the present XRD analysis failed to reveal any additional phases formation and decomposition except the main fcc structure. Further studies are required for the significance of the small volume of different secondary phases to the recrystallization process in the AM CrFeCoNi alloy.

Nevertheless, structural changes with heating of the AM CrFeCoNi alloy can be visible by utilizing the XRD line profiles. The obtained XRD line profiles were analyzed using a William-Hall (W-H) method. The W-H plots with the full width at half maximum (FWHM) against a scattering vector for the CrFeCoNi powder and the AM CrFeCoNi alloy before and after annealing at 400, 700, and 900 °C are presented in Fig. 11a. Table 4 summarizes the obtained results by the XRD analysis as well as subgrain size and dislocation density
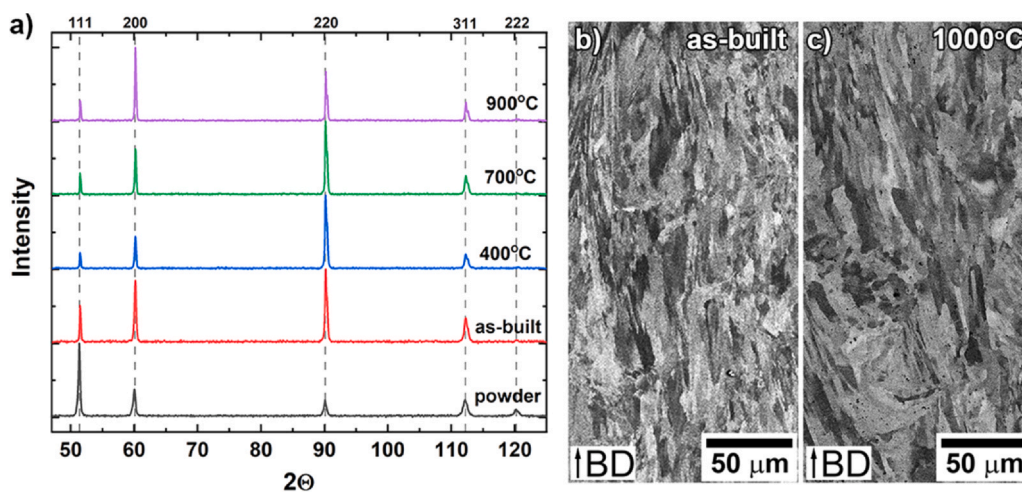

Fig. 10. (a) XRD profiles of the powder and AM CrFeCoNi alloy at as-built condition and annealed at temperatures of 400, 700, and 900 °C for 24 h obtained with a Co-tube; the front view BSE images of (b) as-printed CrFeCoNi alloy and (c) annealed at 1000 °C for 24 h.
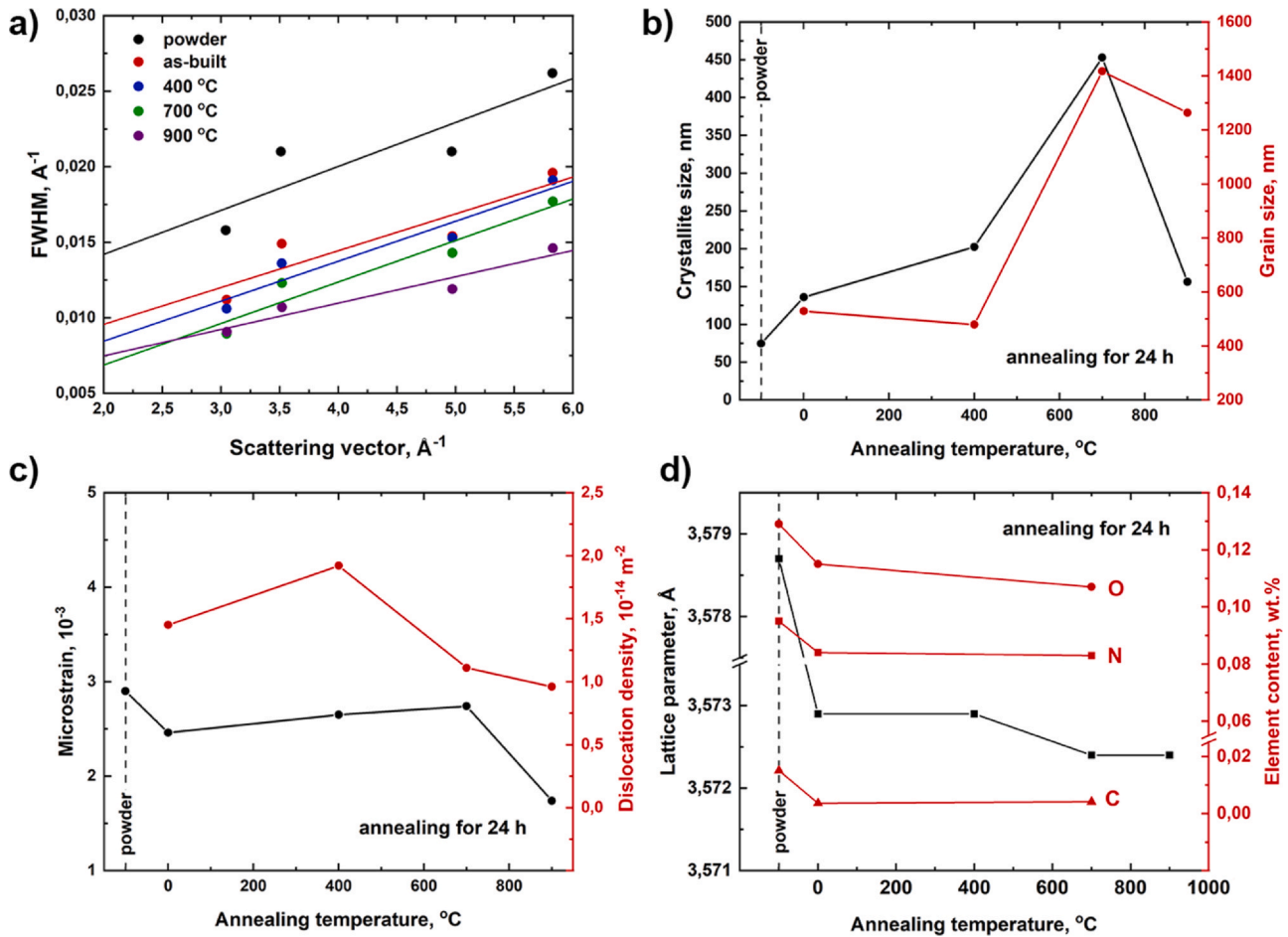
Fig. 11. (a) Williamson-Hall plot with the full width at half maximum (FWHM) against a scattering vector for the CrFeCoNi alloy powder, and the AM CrFeCoNi alloy at as-built and as-annealed at 400, 700, and 900 ℃ conditions; (b) the crystallite size according to W-H analysis and the grain size and (c) the microstrain calculated from XRD profiles and dislocation density for the powder and AM CrFeCoNi alloy at as-built and as-annealed for 24 h conditions; (d) the lattice parameter and light element content in the CrFeCoNi alloy at different conditions. (For interpretation of the references to color in this figure legend, the reader is referred to the web version of this article.)

Table 4
Results of XRD profiles according to W-H method and calculations from TEM analysis.

	Crystallite size, nm	Microstrain	Lattice constant, Å	Dislocation density, $\times 10^{-14}$ m^{-2}	Grain size, nm
powder	74.56	0.00290	3.5787 ± 0.0010	–	–
as-built	136.05	0.00246	3.5729 ± 0.0025	1.45	530
annealed at 400 ℃	202.44	0.00265	3.5729 ± 0.0019	1.92	480
annealed at 700 ℃	452.75	0.00274	3.5724 ± 0.0025	1.11	1420
annealed at 900 ℃	156.24	0.00174	3.5724 ± 0.0032	0.96	1260

estimated by direct microstructural measurements by TEM for the CrFeCoNi alloy. XRD and TEM analyses demonstrate a consistent tendency for the structural sizes to evolve as shown in Fig. 11b. Specifically, similar structural sizes of crystallite and grain size are observed for the as-built and as-annealed samples heated at 400 ℃. These increase dramatically at 400–700 ℃, where the recrystallization process proceeds, and slightly decrease at 900 ℃, which associates with the appearance of recrystallized small grains in the material at 900 ℃. During the recrystallization, following microstructural evolution was observed: i) the cellular substructure transforms to large domains by degradation of the dislocation walls as the subgrain boundaries; and ii) some subgrain boundaries transform to the high-angle boundaries by dislocation absorption. It is worth noting that, although the general trend of the structural sizes is consistent in these two different analyses procedures, the differences often appear due to involved examination sizes, areas,

and volumes where XRD oversees the global sizes and textures, while TEM analysis limits the local microstructures. It is important to note that according to the XRD and microstructure analyses, the texture in the material is observed along BD after annealing at 900–1000 ℃ (Fig. 10). Only after 1200 ℃ annealing, the full recrystallized structure with non-textured equiaxed grains is observed for L-PBF CrFeCoNi alloy [36]. Similar to L-PBF 316l stainless steel [33], the L-PBF CrFeCoNi alloy demonstrates relative structural stability at intermediate temperatures of 800–1000 ℃, which is associated with the features of L-PBF materials. However, additional investigations are required to better understand the grain boundary transformation during the middle- and high-temperature anneals.

Annealing at 400 ℃ leads to an increase in dislocation density as shown in Fig. 11c, and it agrees with the thermal analysis revealing the beginning of the "recovery" peak. At this temperature, the dislocations move from dislocation walls in the subgrain bodies

towards more equilibrium states, resulting in a slight increase of its density. There is an apparent decrease in the microstrain during the heat treatment at 700 and 900 °C, and the reduction of the dislocation density is observed at 700 °C (Fig. 11c). These results confirm the occurrence of a recrystallization process with microstructural relaxation followed by grain growth during heating at 700–900 °C in the AM CrFeCoNi alloy.

4.2. Post printing heating and strengthening

In the present work, effect of annealing temperature on microhardness of the AM CrFeCoNi alloy microhardness was demonstrated in Fig. 3a. A slight increase of microhardness is seen at temperatures of 500–600 °C. Schuh et al. showed a similar hardness behavior for an ultrafine-grained CoCrFeMnNi alloy [10], where the maximum hardness was recorded after annealing at 450 °C for one hour. They suggested there are two possible contributions to the strengthening of the alloy. First, the formation of two new secondary phases having the intermetallics character leads to promotion in strength of the ultrafine-grained CoCrFeMnNi alloy, while the mechanical characteristics were not determined due to a difficulty caused by their small size. Second, there is a reduction of dislocation density upon annealing. The same strengthening behavior was observed in the cold-worked CoCrFeMnNi alloy after one hour annealing at 600 °C which was associated with the bcc and σ particles precipitation [9]. In the present study, increasing hardness during annealing at 500–600 °C for 1 h is presented in Fig. 3b, while the annealing at 600 °C formed the secondary phase only after the long-time heat treatment for 21 days, where the cellular structure persists during heating (Fig. 9b). Moreover, according to DSC analysis, the first endothermic peak for as-built CrFeCoNi alloy associated with the recovery process is observed at 500 °C, where the hardness increases by ~22 HV for the first hour of annealing. It allows the statement that strengthening after short annealing (up to one hour) is initiated due to absorption of dislocations participated in the plastic deformation to grain boundaries and annihilation of dislocations without activating the new dislocation sources. This process puts the dislocations to a more equilibrium statement which requires the additional stress effort to continue the plastic flow. It must be significant in the pre-strained materials, such as AM materials and ultrafine-grained materials.

4.3. Secondary phase formation

It was mentioned earlier that two precipitate types having the $M_{23}C_6$ and M_2N structures were determined in the AM CrFeCoNi alloy through TEM analysis. The $M_{23}C_6$ was observed in several studies for the CrFeCoNi systems at different temperatures [13,35], while no study has described the M_2N for a CoCrFeNi alloy. Hung et al. reveal only the main fcc structure without any additional phases for a CoCrFeNi alloy with > 99.9 wt% purity [12]. The purity of > 99.5 wt% in a CoCrFeNi alloy provides the oxides and carbides [13,37,38]. In the present study, the purity of the CoCrFeNi powder is > 99.7 wt% with the N impurity of ~0.1 wt%. The analysis of a pseudo-binary CoCrFeMnNi−N phase diagram shows the formation of a Cr_2N structure in the fcc matrix starting at ~0.024 wt% at room temperature [39]. Other works also demonstrate the Cr_2N formation in CoCrFeMnNi alloy systems with at least ~0.25 wt% N content and its strengthening effect on the material [40–43]. Due to the similar behavior of CoCrFeMnNi and CrFeCoNi alloys, the N content of ~0.1 wt% is enough for the formation of an M_2N structure. Because of the high cooling rate during the printing process, such structure does not appear at the as-built condition, but, instead, it precipitates during post-printing heat treatment at 700–800 °C and stops at

~900–1000 °C. In practice, the decrease of the N content up to ~0.085 wt% occurs in the material at the printing process with no changes during the heat treatments. However, it can be seen that the O and C contents are also lower in the printed material compared with the powder, Fig. 11d, due to a lower surface area for the solid sample compared with powder. The decrease of the CrFeCoNi lattice parameter after the printing process can be associated with lower contents of light elements in material as shown in Fig. 11d. The further decrease of the lattice parameter after annealings at 700 and 900 °C is explained by the nitrides formation and the N depletion of solid solution.

The effect of secondary phase formation on the mechanical properties was discussed in earlier studies [18,23], where the M_2N precipitates were recognized as a σ-phase. It reveals dramatic effects on the ductile characteristics of the material at cryogenic temperatures and on strengthening under cycling loading. However, the formation of the M_2N precipitates observed at 700 °C annealing does not lead to any strengthening in the present study, as seen from the microhardness test results, due probably to its low content in the bulk samples.

From the present experiments, the following three comments should be noted for further studies. First, the presence of N as an impurity element in the powder leads to the formation of M_2N precipitates in the CrFeCoNi alloy at the temperature range of 700–800 °C, influencing the material properties even if the formation of the precipitates is not significant. Second, no σ-phase was observed in the AM CoCrFeNi alloy after heat treatment up to 1000 °C. As was discussed in the study [12], the solid solution can be achieved as a stable state at higher temperatures up to 1000 °C in the AM CrFeCoNi alloy due to the Mn absence, unlike the CoCrFeMnNi system, where the σ-phase formation initiates at temperatures of 600–900 °C [9–11]. Third, the printing process may decrease the N content. Possibly, the N content in the as-built material can be reduced by manipulating the printing process parameters, as it was demonstrated for high nitrogen steel [44].

5. Conclusions

The analysis of the AM CrFeCoNi alloy with post-printing heat treatment at 400–1000 °C for 24 h and longer time duration was performed in the present work. According to the results, the following statements can be made:

1. The recovery process without recrystallization was observed after heating over 400 °C, and the maximum hardness was observed after one hour annealing at 500 °C. Such hardening is due to the polygonization process beginning when dislocations migrate into grain borders.
2. The recrystallization process followed by grain growth began at and above 600–700 °C, where the hardness drops continuously at 700–1000 °C, while the cellular substructure is observed after long-time heat treatment for 21 days at 600 °C. The structural changes continue with increasing annealing temperature, and the strong texture in the material is observed even after annealing at 900–1000 °C for 24 h.
3. The presence of the nitrogen (~0.09 wt%) in the as-built CrFeCoNi sample tends to form Cr-rich precipitates with an M_2N structure on the grain boundaries after annealing at 700–800 °C, which may affect the mechanical properties of the material, while the microhardness measurement failed to demonstrate additional hardening in the present AM alloy. The long-time heat treatment as low as 600 °C can also lead to secondary phase formation.
4. No σ-phase formation was observed at all investigated temperatures, demonstrating the stable solid solution of the CrFeCoNi system at temperatures up to ~1000 °C.

CRediT authorship contribution statement

Yulia O. Kuzminova: Conceptualization, Methodology, Writing – original draft, Investigation. **Egor A. Kudryavtsev:** Investigation. **Jae-Kyung Han:** Formal analysis. **Megumi Kawasaki:** Writing – review & editing. **Stanislav A. Evlashin:** Resources, Writing – review & editing.

Declaration of Competing Interest

The authors declare that they have no known competing financial interests or personal relationships that could have appeared to influence the work reported in this paper.

Acknowledgments

References

[1] J.W. Yeh, S.K. Chen, S.J. Lin, J.Y. Gan, T.S. Chin, T.T. Shun, C.H. Tsau, S.Y. Chang, Nanostructured high-entropy alloys with multiple principal elements: novel alloy design concepts and outcomes, Adv. Eng. Mater. 6 (2004) 299–303, https://doi.org/10.1002/adem.200300567 (+274).

[2] B. Cantor, I.T.H. Chang, P. Knight, A.J.B. Vincent, Microstructural development in equiatomic multicomponent alloys, Mater. Sci. Eng. A 375–377 (2004) 213–218, https://doi.org/10.1016/j.msea.2003.10.257

[3] D.B. Miracle, O.N. Senkov, A critical review of high entropy alloys and related concepts, Acta Mater. 122 (2017) 448–511, https://doi.org/10.1016/j.actamat.2016.08.081

[4] M.A. Hemphill, T. Yuan, G.Y. Wang, J.W. Yeh, C.W. Tsai, A. Chuang, P.K. Liaw, Fatigue behavior of Al 0. 5 CoCrCuFeNi high entropy alloys, Acta Mater. 60 (2012) 5723–5734, https://doi.org/10.1016/j.actamat.2012.06.046

[5] B.B. Bian, N. Guo, H.J. Yang, R.P. Guo, L. Yang, Y.C. Wu, J.W. Qiao, A novel cobalt-free FeMnCrNi medium-entropy alloy with exceptional yield strength and ductility at cryogenic temperature, J. Alloy. Compd. 827 (2020) 153981, https://doi.org/10.1016/j.jallcom.2020.153981

[6] D. Liu, X. Jin, N. Guo, P.K. Liaw, J.W. Qiao, Non-equiatomic FeMnCrNiAl high-entropy alloys with heterogeneous structures for strength and ductility combination, Mater. Sci. Eng.: A 818 (2021) 141386, https://doi.org/10.1016/j.msea.2021.141386

[7] H.-P. Chou, Y.-S. Chang, S.-K. Chen, J.-W. Yeh, Microstructure, thermophysical and electrical properties in AlxCoCrFeNi (0 ≤ x ≤2) high-entropy alloys, Mater. Sci. Eng. B 163 (2009) 184–189, https://doi.org/10.1016/J.MSEB.2009.05.024

[8] T.S. Reddy, I.S. Wani, T. Bhattacharjee, S.R. Reddy, R. Saha, P.P. Bhattacharjee, Intermetallics Severe plastic deformation driven nanostructure and phase evolution in a Al 0. 5 CoCrFeMnNi dual phase high entropy alloy, Intermetallics 91 (2017) 150–157, https://doi.org/10.1016/j.intermet.2017.09.002

[9] M.V. Klimova, D.G. Shaysultanov, S.V. Zherebtsov, N.D. Stepanov, Effect of second phase particles on mechanical properties and grain growth in a CoCrFeMnNi high entropy alloy, Mater. Sci. Eng. A 748 (2019) 228–235, https://doi.org/10.1016/j.msea.2019.01.112

[10] B. Schuh, F. Mendez-Martin, B. Völker, E.P. George, H. Clemens, R. Pippan, A. Hohenwarter, Mechanical properties, microstructure and thermal stability of a nanocrystalline CoCrFeMnNi high-entropy alloy after severe plastic deformation, Acta Mater. 96 (2015) 258–268, https://doi.org/10.1016/J.ACTAMAT.2015.06.025

[11] F. Otto, A. Dlouhý, K.G. Pradeep, M. Kuběnová, D. Raabe, G. Eggeler, E.P. George, Decomposition of the single-phase high-entropy alloy CrMnFeCoNi after prolonged anneals at intermediate temperatures, Acta Mater. 112 (2016) 40–52, https://doi.org/10.1016/j.actamat.2016.04.005

[12] P.T. Hung, M. Kawasaki, J.-K. Han, J.L. Lábár, J. Gubicza, Microstructure evolution in a nanocrystalline CoCrFeNi multi-principal element alloy during annealing, Mater. Charact. 171 (2021) 110807, https://doi.org/10.1016/j.matchar.2020.110807

[13] P. Sathiyamoorthi, J. Basu, S. Kashyap, K.G. Pradeep, R. Sankar, Thermal stability and grain boundary strengthening in ultra fi ne-grained CoCrFeNi high entropy alloy composite, Mater. Des. 134 (2017) 426–433, https://doi.org/10.1016/j.matdes.2017.08.053

[14] S. Praveen, B.S. Murty, R.S. Kottada, Alloying behavior in multi-component AlCoCrCuFe and NiCoCrCuFe high entropy alloys, Mater. Sci. Eng. A 534 (2012) 83–89, https://doi.org/10.1016/j.msea.2011.11.044

[15] C. Juan, M. Tsai, C. Tsai, C. Lin, W. Wang, C. Yang, S. Chen, S. Lin, J. Yeh, Intermetallics Enhanced mechanical properties of HfMoTaTiZr and HfMoNbTaTiZr refractory high-entropy alloys, Intermetallics 62 (2015) 76–83, https://doi.org/10.1016/j.intermet.2015.03.013

[16] H. Chen, A. Kauffmann, S. Laube, I. Choi, R. Schwaiger, Y. Huang, K. Lichtenberg, F. Mu, Contribution of lattice distortion to solid solution strengthening in a series of refractory high entropy alloys, n.d., doi: 10.1007/s11661-017-4386-1.

[17] A. Riemer, S. Leuders, M. Thöne, H.A. Richard, T. Tröster, T. Niendorf, On the fatigue crack growth behavior in 316L stainless steel manufactured by selective laser melting, Eng. Fract. Mech. 120 (2014) 15–25, https://doi.org/10.1016/j.engfracmech.2014.03.008

[18] Y. Kuzminova, D. Firsov, A. Dudin, S. Sergeev, A. Zhilyaev, A. Dyakov, A. Chupeeva, A. Alekseev, D. Martynov, I. Akhatov, S. Evlashin, The effect of the parameters of the powder bed fusion process on the microstructure and mechanical properties of CrFeCoNi medium-entropy alloys, Intermetallics 116 (2020) 106651, https://doi.org/10.1016/j.intermet.2019.106651

[19] R. Li, P. Niu, T. Yuan, P. Cao, C. Chen, K. Zhou, Selective laser melting of an equiatomic CoCrFeMnNi high-entropy alloy: processability, non-equilibrium microstructure and mechanical property, J. Alloy. Compd. 746 (2018) 125–134, https://doi.org/10.1016/j.jallcom.2018.02.298

[20] Y. Chew, G.J. Bi, Z.G. Zhu, F.L. Ng, F. Weng, S.B. Liu, S.M.L. Nai, B.Y. Lee, Microstructure and enhanced strength of laser aided additive manufactured CoCrFeNiMn high entropy alloy, Mater. Sci. Eng. A 744 (2019) 137–144, https://doi.org/10.1016/j.msea.2018.12.005

[21] C. Haase, F. Tang, M.B. Wilms, A. Weisheit, B. Hallstedt, Combining thermodynamic modeling and 3D printing of elemental powder blends for high-throughput investigation of high-entropy alloys – towards rapid alloy screening and design, Mater. Sci. Eng. A 688 (2017) 180–189, https://doi.org/10.1016/j.msea.2017.01.099

[22] Y. Brif, M. Thomas, I. Todd, The use of high-entropy alloys in additive manufacturing, Scr. Mater. 99 (2015) 93–96, https://doi.org/10.1016/j.scriptamat.2014.11.037

[23] Y.O. Kuzminova, D.G. Firsov, S.A. Dagesyan, S.D. Konev, S.N. Sergeev, A.P. Zhilyaev, M. Kawasaki, I.S. Akhatov, S.A. Evlashin, Fatigue behavior of additive manufactured CrFeCoNi medium-entropy alloy, J. Alloy. Compd. 863 (2021) 158609, https://doi.org/10.1016/j.jallcom.2021.158609

[24] W. Zhao, J.-K. Han, Y.O. Kuzminova, S.A. Evlashin, A.P. Zhilyaev, A.M. Pesin, J. Jang, K.-D. Liss, M. Kawasaki, Significance of grain refinement on micro-mechanical properties and structures of additively-manufactured CoCrFeNi high-entropy alloy, Mater. Sci. Eng.: A 807 (2021) 140898, https://doi.org/10.1016/j.msea.2021.140898

[25] D. Lin, L. Xu, Y. Han, Y. Zhang, H. Jing, Structure and mechanical properties of a FeCoCrNi high-entropy alloy fabricated via selective laser melting, Intermetallics 127 (2020) 106963, https://doi.org/10.1016/j.intermet.2020.106963

[26] J. Joseph, T. Jarvis, X. Wu, N. Stanford, P. Hodgson, D.M. Fabijanic, Comparative study of the microstructures and mechanical properties of direct laser fabricated and arc-melted AlxCoCrFeNi high entropy alloys, Mater. Sci. Eng. A 633 (2015) 184–193, https://doi.org/10.1016/j.msea.2015.02.072

[27] M. Li, J. Gazquez, A. Borisevich, R. Mishra, K.M. Flores, Evaluation of microstructure and mechanical property variations in AlxCoCrFeNi high entropy alloys produced by a high-throughput laser deposition method, Intermetallics 95 (2018) 110–118, https://doi.org/10.1016/j.intermet.2018.01.021

[28] A.M. Filimonov, O.A. Rogozin, D.G. Firsov, Y.O. Kuzminova, S.N. Sergeev, A.P. Zhilyaev, M.I. Lerner, N.E. Toropkov, A.P. Simonov, I.I. Binkov, I.V. Okulov, I.S. Akhatov, S.A. Evlashin, Hardening of additive manufactured 316L stainless steel by using bimodal powder containing nanoscale fraction, Materials 14 (2020) 115, https://doi.org/10.3390/ma14010115

[29] A. Bowman, G. Arnold, E. Storms, N. Nereson, The crystal structure of Cr23C6, Acta Crystallogr. Sect. B Struct. Crystallogr. Cryst. Chem. 28 (10) (1972) 3102–3103, https://doi.org/10.1107/S0567740872007526

[30] Y.M. Wang, T. Voisin, J.T. McKeown, J. Ye, N.P. Calta, Z. Li, Z. Zeng, Y. Zhang, W. Chen, T.T. Roehling, R.T. Ott, M.K. Santala, P.J. Depond, M.J. Matthews, A.V. Hamza, T. Zhu, Additively manufactured hierarchical stainless steels with high strength and ductility, Nat. Mater. 17 (2018) 63–71, https://doi.org/10.1038/nmat5021

[31] R. Wu, M. Zaiser, Cell structure formation in a two-dimensional density-based dislocation dynamics model, Mater. Theory 5 (2021) 3, https://doi.org/10.1186/s41313-020-00025-x

[32] R. Wu, D. Tüzes, P.D. Ispánovity, I. Groma, T. Hochrainer, M. Zaiser, Instability of dislocation fluxes in a single slip: deterministic and stochastic models of dislocation patterning, Phys. Rev. B 98 (2018) 054110, https://doi.org/10.1103/PhysRevB.98.054110

[33] T. Voisin, J.-B. Forien, A. Perron, S. Aubry, N. Bertin, A. Samanta, A. Baker, Y.M. Wang, New insights on cellular structures strengthening mechanisms and thermal stability of an austenitic stainless steel fabricated by laser powder-bed-fusion, Acta Mater. 203 (2021) 116476, https://doi.org/10.1016/j.actamat.2020.11.018

[34] J. Cabana, C.D. Ling, J. Oró-Solé, D. Gautier, G. Tobías, S. Adams, E. Canadell, M.R. Palacín, Antifluorite-type lithium chromium oxide nitrides: synthesis, structure, order, and electrochemical properties, Inorg. Chem. 43 (2004) 7050–7060, https://doi.org/10.1021/ic049138z

[35] T.-T. Shun, Y.-C. Du, Age hardening of the Al0.3CoCrFeNiC0.1 high entropy alloy, J. Alloy. Compd. 478 (2009) 269–272, https://doi.org/10.1016/j.jallcom.2008.12.014

[36] Y. Kuzminova, A. Shibalova, S. Evlashin, I. Shishkovsky, P. Krakhmalev, Structural effect of low Al content in the in-situ additive manufactured CrFeCoNiAlx high-entropy alloy, Mater. Lett. 303 (2021) 130487, https://doi.org/10.1016/j.matlet.2021.130487

[37] S. Praveen, B.S. Murty, R.S. Kottada, Phase evolution and densification behavior of nanocrystalline multicomponent high entropy alloys during spark plasma sintering, JOM 65 (2013) 1797–1804, https://doi.org/10.1007/s11837-013-0759-0

[38] S. Praveen, J. Basu, S. Kashyap, R. Sankar, Exceptional resistance to grain growth in nanocrystalline CoCrFeNi high entropy alloy at high homologous temperatures, J. Alloy. Compd. 662 (2016) 361–367, https://doi.org/10.1016/j.jallcom.2015.12.020

[39] Igor Moravcik, Jan Cizek, Larissa dA. Gouvea, Jan Cupera, Ivan Guban, Ivo Dlouhy, Nitrogen interstitial alloying of CoCrFeMnNi high entropy alloy through reactive powder milling, Entropy 21 (4) (2019) 363, https://doi.org/10.3390/e21040363

[40] F. Xiong, R. Fu, Y. Li, D. Sang, Effects of nitrogen alloying and friction stir processing on the microstructures and mechanical properties of CoCrFeMnNi high-entropy alloys, J. Alloy. Compd. 822 (2020) 153512, https://doi.org/10.1016/j.jallcom.2019.153512

[41] D. Edgard, J. Park, B. Straumal, N. Park, Investigation on the precipitate formation and behavior in nitrogen-containing equiatomic CoCrFeMnNi high-entropy alloy, Mater. Lett. 258 (2020) 126806, https://doi.org/10.1016/j.matlet.2019.126806

[42] D. Edgard, J. Park, N. Park, Strengthening of ultrafine-grained equiatomic CoCrFeMnNi high-entropy alloy by nitrogen addition, Mater. Lett. 258 (2020) 126772, https://doi.org/10.1016/j.matlet.2019.126772

[43] M. Klimova, D. Shaysultanov, A. Semenyuk, S. Zherebtsov, G. Salishchev, N. Stepanov, Effect of nitrogen on mechanical properties of CoCrFeMnNi high entropy alloy at room and cryogenic temperatures, J. Alloy. Compd. 849 (2020) 156633, https://doi.org/10.1016/j.jallcom.2020.156633

[44] A. Arabi-hashemi, X. Maeder, R. Figi, C. Schreiner, S. Griffiths, C. Leinenbach, 3D magnetic patterning in additive manufacturing via site-specific in-situ alloy modification, Appl. Mater. Today 18 (2020) 100512, https://doi.org/10.1016/j.apmt.2019.100512